September 1993

Resonant two-color detachment of H^- with excitation of H(n=2)

Ning-Yi Du
University of Colorado, Boulder

Anthony F. Starace
University of Nebraska-Lincoln, astarace1@unl.edu

N.A. Cherepkov
University of Nebraska - Lincoln

Resonant two-color detachment of H^- with excitation of $H(n = 2)$

Ning-Yi Du* and Anthony F. Starace†

Joint Institute for Laboratory Astrophysics, University of Colorado, Boulder, Colorado 80309-0440 and National Institute of Standards and Technology, Boulder, Colorado 80303

N. A. Cherepkov‡

Department of Physics and Astronomy, The University of Nebraska, Lincoln, Nebraska 68588-0111

(Received 2 September 1992)

The cross sections for resonant two-color, two-photon detachment of H^- with excitation of the degenerate $H(2s)$ and $H(2p)$ levels are calculated within a semiempirical adiabatic hyperspherical representation. The first photon, with energy $\omega_1 = 0.4017$ a.u., is resonant with the well-known Feshbach $^1P^o$ resonance below the $H(n = 2)$ threshold. The second photon, with energy $\omega_2 \geq 0.126\,05$ a.u., scans the energy region above the $H(n = 2)$ threshold over which long-range dipole-field-induced cross-section oscillations are predicted to occur. Such Gailitis-Damburg oscillations have not yet been observed experimentally. Results for various pairs of light polarization for the two photons are presented. Our resonant two-color, two-photon detachment cross sections are 8–9 orders of magnitude greater than the corresponding nonresonant, single-color, two-photon detachment cross sections obtained by Liu, Du, and Starace [Phys. Rev. A **43**, 5891 (1991)]. Unmistakable evidence of long-range dipole-field effects is presented over the 5-meV energy range above the $H(n = 2)$ threshold. Furthermore, the differential cross sections for right- and left-circularly polarized, copropagating photons and especially the circular dichroism differential cross sections are shown to have nearly a full cycle of a greatly enhanced dipole-field-induced oscillation extending over the region from threshold to ≈ 34 meV above.

PACS number(s): 32.80.Wr

I. INTRODUCTION

The dipole interaction between an electron and the degenerate $H(2s)$ and $H(2p)$ energy levels can result in an attractive long-range potential in particular channels [1]. Processes involving transitions to these channels have been shown theoretically to have finite cross sections at threshold, which oscillate above threshold [2]. Such Gailitis-Damburg oscillations [2] have never been observed experimentally, however. Indeed, until recently such oscillations in the cross section were expected to be strongly suppressed above threshold [3, 4].

More recent theoretical work has indicated ways in which these long-range, dipole-field-induced oscillations may be observed. Liu and Starace [5] have pointed out that such oscillations are in general not suppressed in differential cross sections, which are sensitive to phase-interference effects between different channels. They predicted [5(a)] sizable dipole-field-induced oscillations in the angular distributions for collisional detachment of H^- accompanied by excitation of $H(n = 2)$. However, for this process the intense shape resonance feature at 18 meV above threshold in one of the $^1P^o$ final-state channels obscures these oscillations in the meV energy region. These predicted sizable oscillations can only therefore be observed in the collisional detachment process in the energy region below ≈ 1 meV above threshold in the H^- reference frame. Such low-energy features of the $H(n = 2)$-e^- system appear on a much larger energy scale in the laboratory frame, but are concentrated in the forward direction [5].

Liu, Du, and Starace [6] have pointed out that the obscuring effect of the intense $^1P^o$ shape resonance feature can be avoided by studying two-photon detachment of H^- accompanied by excitation of $H(n = 2)$. Electric dipole selection rules, for example, restrict the allowed final states to have even parity. Furthermore, the $^1D^e+$ final-state channel of the $H(n = 2)$-e^- system, which is populated in two-photon detachment of H^-, was shown to have quite sizable dipole-field-induced oscillations in its cross section over an energy range extending from threshold to about 34 meV above [6]. Of course, as is true for any nonresonant two-photon process, the cross section for populating the $^1D^e+$ channel is small.

In this paper we present semiempirical, adiabatic hyperspherical theoretical calculations for resonant, two-color, two-photon detachment of H^- with excitation of $H(n = 2)$. One of the photons is chosen to have an energy in resonance with the lowest $^1P^o$ Feshbach resonance below the $H(n = 2)$ threshold. The other is chosen to scan the energy region above threshold. We predict that these resonant two-color, two-photon detachment cross sections are nine orders of magnitude larger than the nonresonant, single-color, two-photon detachment cross sections studied previously [6]. However, because the $^1P^o$ Feshbach resonance is so close to the $H(n = 2)$ threshold, it has a very large radial extent. In general, this fact restricts the energy over which dipole-field-induced

oscillations in the total cross sections are unmistakable to a much smaller energy region than in the nonresonant, two-photon process studied previously [6]. Nevertheless, the partial differential cross sections show unmistakable effects of the long-range, dipole field over a large energy region from threshold up to 100 meV or more in certain cases. Furthermore, the two-color process allows us to examine the influence of alternative polarizations for the two photons. In particular, when the first photon is circularly polarized, it causes the resonant intermediate state to be oriented, and hence for this state there is a nonzero circular dichroism effect [7].

In Sec. II we review briefly our theoretical approach, discussing both our semiempirical adiabatic hyperspherical method and the long-range dipole-field-induced effects to be examined. In Sec. III we present expressions for the resonant two-color detachment cross sections for three different pairs of light polarization and examine the magnitude of the circular dichroism effect. For simplicity we restrict our considerations to the case in which the characteristic light polarization vectors are collinear. In Sec. IV we present our results and in Sec. V we discuss our results and give our conclusions. In the Appendix we specify which other channels converging to excited states n of the H(n)-e^- system are expected to have significant dipole-field oscillations above threshold.

II. GENERAL THEORETICAL ASPECTS

In this paper we are concerned with the process of resonant two-color detachment of H^- with excitation of the H($n=2$) state, i.e.,

$$H^- + \gamma_1 + \gamma_2 \rightarrow H(n=2) + e^- , \tag{1}$$

where γ_1 is resonant in energy with the lowest-energy $^1P^o$ Feshbach resonance of H^- below the H($n=2$) threshold. Due to the degeneracy of the H($2s$) and H($2p$) states, the final state of this process is influenced by the long-range dipole-field interaction between the H atom and the detached electron. We first describe these effects and then examine the process (1) in particular. Since a more detailed description of our general approach has been presented in Ref. [6], we emphasize here those key aspects needed to properly interpret our results.

A. Low-energy states of the H($n=2$)-e^- system

In our calculations we describe the H($n=2$)-e^- three-body system in an adiabatic hyperspherical representation [8–10] since this is known to describe fairly accurately the key dynamical features of this system [11] and since this representation is known to diagonalize asymptotically the long-range dipole interaction for this system [8, 11].

In the hyperspherical approach the exact two-electron wave function $\psi(\mathbf{r}_1, \mathbf{r}_2)$ is expanded in a complete set of adiabatic eigenfunctions $\phi_\mu(R, \alpha, \hat{\mathbf{r}}_1, \hat{\mathbf{r}}_2)$, which depend parametrically on a hyperradius $R \equiv (r_1^2 + r_2^2)^{1/2}$ and are functions of the five angular variables $\alpha \equiv \tan^{-1}(r_2/r_1)$, $\hat{\mathbf{r}}_1$ and $\hat{\mathbf{r}}_2$:

$$\psi(R, \alpha, \hat{\mathbf{r}}_1, \hat{\mathbf{r}}_2) \equiv [R^{5/2}\sin(\alpha)\cos\alpha]^{-1} \times \sum_\mu F_\mu(R)\phi_\mu(R, \alpha, \hat{\mathbf{r}}_1, \hat{\mathbf{r}}_2) . \tag{2}$$

The ϕ_μ satisfy an angular equation [8–10] having an eigenvalue $U_\mu(R)$. The F_μ satisfy a set of coupled radial equations [8–10]; however, in the adiabatic approximation all but the diagonal coupling matrix elements are dropped so that each $F_\mu(R)$ satisfies a one-dimensional radial Schrödinger equation,

$$\left[\frac{d^2}{dR^2} - V_\mu(R) + k^2\right] F_{\mu k}(R) = 0 . \tag{3}$$

(The effect of nonadiabatic coupling on the ground-state radial wave function is discussed in Sec. IV B.) In Eq. (3) the effective radial potential $V_\mu(R)$, which characterizes the dynamical features of a particular hyperspherical channel μ converging to the nth level of the H atom is defined by

$$-V_\mu(R) \equiv \frac{U_\mu(R) + \frac{1}{4}}{R^2} + \left(\phi_\mu, \frac{d^2\phi_\mu}{dR^2}\right) - \frac{1}{n^2} , \tag{4}$$

where $(\phi_\mu, d^2\phi_\mu/dR^2)$ is the R-dependent diagonal coupling matrix element for the μth channel. Since the long-range dipole interaction due to the degeneracy of the H($n=2$) states [1] is diagonal in the hyperspherical representation [8, 11], the asymptotic form of the effective radial potential is

$$V_\mu(R) \underset{R\to\infty}{\simeq} \lambda_\mu(\lambda_\mu + 1)/R^2 . \tag{5}$$

In Eq. (5) λ_μ is an effective orbital angular momentum, which may be real or complex depending on the channel μ. For channels μ in which the long-range dipole interaction [1] is repulsive at asymptotic distances, λ_μ is real. Hence at threshold the cross section for any excitation to the channel μ is zero since it depends on $|k^{\lambda_\mu+1/2}|^2$, which is zero for $k \rightarrow 0$. On the other hand, for channels μ in which the long-range dipole interaction [1] is attractive at asymptotic distances, one may write quite generally [12]

$$\lambda_\mu = -\tfrac{1}{2} + i\alpha_\mu . \tag{6}$$

As a consequence, the threshold value of the cross section for any excitation to the channel μ is finite [2] since it depends on $|k^{\lambda_\mu+1/2}|^2 = 1$. In addition, as noted by Gailitis and Damburg [2], the transition matrix elements for channels having complex λ_μ are influenced above threshold by the term $k^{\lambda_\mu+1/2} = k^{i\alpha_\mu}$ [cf. Eq. (6)], which, when rewritten as $\exp(i\alpha_\mu \ln k)$, may be seen to oscillate as a function of $\ln k$.

Some of the effective potentials $V_\mu(R)$ that converge asymptotically to the H($n=2$) threshold are shown in Fig. 1. All of the $^1S^e$ and $^1P^o$ potential curves are shown as well as the most important $^1D^e$ potential curve. Since the total orbital and spin angular momenta are insufficient to specify the potential curves uniquely, additional specification is necessary. In Fig. 1 we have employed abbreviated labels corresponding to Lin's classification of doubly excited states [13].

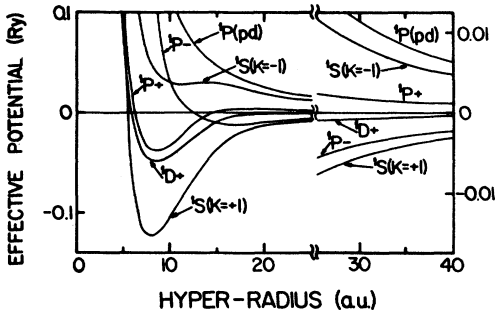

FIG. 1. Effective radial hyperspherical potentials V_μ in rydbergs plotted vs the hyperradius R for six channels converging to H($n = 2$): $^1S(K = \pm 1)$, $^1P\pm$, $^1P(pd)$, and $^1D+$. Note that the zero of energy is chosen to be the H($n = 2$) threshold and that near R=25 the vertical energy scale is changed.

The key features of the interactions within the H($n = 2$)-e^- system are clearly exhibited in the effective potential curves shown in Fig. 1. These are, first, that the $^1P+$ potential is attractive at short distances and weakly repulsive at large distances, thereby giving rise to a *shape resonance* (which is seen experimentally at about 18 meV above threshold) [11]. This shape resonance feature dominates the cross section of any process that populates the $^1P^o$ final-state channels above the H($n = 2$) threshold.

Second, because of their long-range repulsive behavior, the $^1P+$, $^1P(pd)$, and $^1S(K = -1)$ potentials all have *zero cross sections at threshold.* Third, the three potentials corresponding to the $^1S(K = +1)$, $^1P-$, and $^1D+$ channels are attractive at asymptotic distances. As discussed above, they therefore have complex effective angular momenta. Hence the excitation cross section for each of these channels is *finite at threshold* [within the center-of-mass frame of the H($n = 2$)-e^- system]. Furthermore, the transition amplitudes for excitations to these three channels *oscillate on a ln k scale above threshold* [2].

B. Two-photon detachment of H⁻ with excitation of H($n = 2$)

The two-photon detachment process in Eq. (1) is a very favorable one for observing Gailitis-Damburg oscillations [2] above the H($n = 2$) threshold [6]. This is so for two reasons. First, electric dipole selection rules do not permit population of $^1P^o$ final-state channels. Hence the strong shape resonance in the $^1P+$ final-state channel about 18 meV above threshold cannot obscure these near-threshold oscillations. Second, the two-photon process does populate $^1S^e$ and $^1D^e$ final-state channels, one of which, the $^1D+$ channel, is the only one converging to the H($n = 2$) threshold having significant, undamped oscillations above threshold [6].

In calculating these Gailitis-Damburg oscillations [2] for this process, we must ask how we can be sure that the wiggles our calculations give for the two-photon detachment plus excitation cross sections of H⁻ are really due to long-range dipole-field effects and are not due to some other cause. The answer is that the generalized quantum-defect theory (QDT) of Greene, Fano, and Strinati [12] for a long-range dipole field enables us to disentangle dipole-field effects from our numerical results *analytically.* In this way we are able to state with assurance which features of our cross-section results are truly the Gailitis-Damburg oscillations [2] and which features are energy-dependent wiggles arising from other causes.

Through use of the QDT for long-range dipole fields [12] one may show that our adiabatic hyperspherical radial functions, defined by Eq. (3), tend asymptotically to

$$F_{\mu k}(R) \underset{R\to\infty}{\simeq} (2/\pi k)^{1/2} \sin(kR + \xi_\mu + \eta_\mu) , \tag{7}$$

where η_μ is the short-range phase shift in the μth channel and the ξ_μ is an analytically known phase dependent on the effective angular momentum λ_μ characterizing the long-range dipole interaction of the H($n = 2$)-e^- system [12]. For real values of λ_μ,

$$\xi_\mu \equiv -\tfrac{1}{2}\pi\lambda_\mu , \tag{8}$$

while for complex values of λ_μ,

$$\xi_\mu \equiv -\tfrac{1}{4}\pi + \theta_\mu , \tag{9}$$

where

$$\theta_\mu \equiv -\tan^{-1} \frac{\tan[\alpha_\mu \ln(k/2) + x_\mu]}{\tanh(\pi\alpha_\mu/2)} \tag{10}$$

and

$$x_\mu \equiv \arg\Gamma(1 - i\alpha_\mu) . \tag{11}$$

The generalized QDT may also be used to extract the long-range dipole-field-induced energy dependence of $F_{\mu k}(R)$ by representing our adiabatic hyperspherical radial wave functions as [14]

$$F_{\mu k}(R) = N_\mu(k) F^0_{\mu k}(R), \tag{12}$$

where $N_\mu(k)$ is an effective normalization factor that determines essentially all of the energy dependence of the radial wave function near $R \approx 0$, and where $F^0_{\mu k}(R)$ is a more smoothly varying function of k. The oscillatory, energy-dependent normalization factor $N_\mu(k)$ is an analytically known function of $\ln k$ [6, 14].

There are two major ways in which an attractive dipole field introduces oscillations in measured cross sections on a $\ln k$ energy scale. The first is due to the rapid variation of the analytically determined dipole phase θ_μ [cf. Eqs. (9) and (10)] for those hyperspherical channels μ having complex values of the effective angular momentum λ_μ. This analytically determined phase θ_μ (through ξ_μ) appears explicitly in the phase factor included in the two-photon transition amplitudes [6]. Interference effects between different amplitudes, such as occur commonly in calculating the angular distributions for the detached electrons, generally lead to sizable, undamped oscillations in the corresponding cross sections due to the rapid decrease of the analytically determined phases θ_μ with increasing $\ln k$. This behavior is shown in Fig. 2 for all three channels having complex λ_μ above the H($n = 2$) threshold.

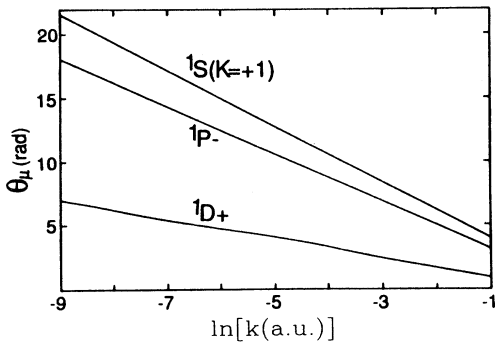

FIG. 2. Analytically known phases θ_μ [defined in Eq. (10)] vs ln k, where k (a.u.) is the detached-electron momentum, for the three adiabatic hyperspherical channels $\mu = {}^1S(K{=}+1)$, ${}^1P-$, and ${}^1D+$.

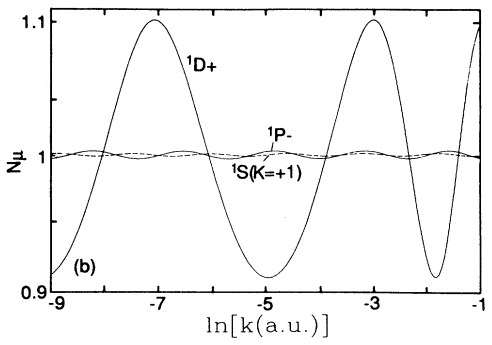

FIG. 3. Normalization factors $N_\mu(k)$ [cf. Eq. (12)] for the three adiabatic hyperspherical channels $\mu = {}^1S(K{=}+1)$, ${}^1P-$, and ${}^1D+$ vs ln k, where k is the detached-electron momentum.

The second major way the long-range dipole field introduces oscillations in the cross sections is through the effective normalization $N_\mu(k)$ introduced in Eq. (12). Its behavior is shown in Fig. 3 for each of the three channels above the H($n = 2$) threshold having complex λ_μ. One sees clearly that whereas the long-range dipole-field-induced oscillations of $N_\mu(k)$ for the ${}^1S(K = +1)$ and ${}^1P-$ channels are strongly damped [3, 4], those for the ${}^1D+$ channel are quite sizable [6]. The amplitude of these oscillations depends sensitively on the value of α_μ, the complex part of the effective angular momentum λ_μ [cf. Eq. (6)] [3, 4, 15]. In the Appendix to this paper we indicate all channels of the H(n)-e^- system for which such oscillations have an amplitude exceeding 10%. We have found only eight such channels in a search that considered principal quantum numbers n in the range $2 \le n \le 15$ and total orbital angular momentum L in the range $0 \le L \le 3$.

III. FORMULAS FOR RESONANT, TWO-COLOR DETACHMENT CROSS SECTIONS

As already stated, a detailed description of our theoretical approach has been presented in Ref. [6]. In Sec. II of this paper the key physical aspects of the detachment plus excitation process in Eq. (1) have been discussed. In this section we specify those modifications of the formulas presented in Ref. [6] that arise due to the resonant nature of process (1) and due to the use of two different frequency photons having possibly different polarizations.

A. Two-photon transition amplitudes

If we characterize the resonant intermediate state in process (1) by its complex energy $E_r + i\frac{1}{2}\Gamma_r$, where Γ_r is its width, then the two-photon transition amplitude defined in Eq. (20) of Ref. [6] becomes

$$T^{(2)}_{n\ell m\mathbf{k}} \equiv -i2\Gamma_r^{-1}\,\langle\Psi^-_{n\ell m\mathbf{k}}|D^1_{q'}|\Psi_{\mu_r}\rangle\langle\Psi_{\mu_r}|D^1_q|\Psi_0\rangle\,. \tag{13}$$

We have assumed in Eq. (13) that the first photon's frequency is exactly on resonance, i.e., $\omega \equiv E_r - E_0$. Also, the electric dipole operator D^1_q is defined by

$$D^1_q \equiv \hat{\boldsymbol{\epsilon}}_q \cdot \sum_{i=1}^{2} \mathbf{r}_i\,, \tag{14}$$

where $\hat{\boldsymbol{\epsilon}}_q$ is the polarization vector of the photon expressed in spherical tensor form in which $q = +1$ (-1) for right- (left-) circularly polarized light and in which $q = 0$ for linearly polarized light.

The initial-state wave function for H^- in Eq. (13) is given in the adiabatic hyperspherical approximation by

$$\psi_0(\mathbf{r}_1,\mathbf{r}_2) = [R^{5/2}\cos(\alpha)\sin\alpha]^{-1} \times\Phi_{\mu=0}(R,\alpha,\hat{\mathbf{r}}_1\,,\hat{\mathbf{r}}_2)F_{\mu=0}(R)\,, \tag{15}$$

where $\mu = 0$ is the lowest adiabatic hyperspherical ${}^1S$ channel; its potential converges asymptotically to the H($n = 1$) threshold. $\Phi_{\mu=0}$ becomes proportional to the H($1s$) wave function as $r_1 \to \infty$. $F_{\mu=0}(R)$ is the lowest-energy radial solution for the $\mu = 0$ ${}^1S$ potential.

The intermediate state wave function $\Psi_{\mu_r}(\mathbf{r}_1,\mathbf{r}_2)$ in Eq. (13) has a form identical to that of Eq. (15), except for a different index μ_r, which denotes the ${}^1P-$ channel converging to the H($n = 2$) threshold whose radial potential is shown in Fig. 1. $F_{\mu_r}(R)$ is the lowest-energy radial solution for this $\mu_r \equiv {}^1P-$ potential.

The incoming-wave-normalized wave function in Eq. (13) describing the final state in which asymptotically the H atom is excited to its nlm level and the detached electron departs with relative momentum $\mathbf{k}$ is defined by

$$\Psi^-_{nlm\mathbf{k}}(\mathbf{r}_1,\mathbf{r}_2) = k^{-1/2}\sum_{l',m'}\sum_{L,M}\sum_{\mu}\Psi^-_{\mu k}(R,\alpha,\hat{\mathbf{r}}_1,\hat{\mathbf{r}}_2)\,e^{-i\xi_\mu}\,A^\dagger_{\mu,(ll')}\,\langle LM|lml'm'\rangle\,Y^*_{l'm'}(\hat{\mathbf{k}})\,. \tag{16}$$

Here $\Psi^-_{\mu k}$ is an incoming-wave-normalized hyperspherical wave function for the channel μ, where k is defined by

$$\tfrac{1}{2}k^2 \equiv E_0 + \omega + \omega' + \frac{1}{2n^2} . \tag{17}$$

ξ_μ is the analytically determined phase characteristic of the channel μ [cf. Eqs. (8)–(11)]. The matrix $A^\dagger_{\mu,(ll')}$ transforms the dipole-field channels μ to the independent electron channels ll' characterized by the orbital angular momenta l and l' of the H atom electron and the detached electron, respectively. The channel index μ designates implicitly the total orbital and spin angular momenta, LS, of the final state, although this fact is not made explicit in Eq. (16) for simplicity of notation. Similarly, the dependence of the wave function $\Psi^-_{\mu k}$ on the magnetic quantum numbers M and M_S corresponding to L and S is also suppressed. The Clebsch-Gordan coefficient projects the total orbital angular momentum state $\langle LM|$ onto the independent electron state $|lml'm'\rangle$, while the spherical harmonic projects the detached-electron state $\langle l'm'|$ onto the state having momentum direction $\hat{\mathbf{k}}$. The prefactor k^{-1} in Eq. (16) is needed to ensure normalization of the wave function in Eq. (16) to a δ function in electron momentum $\mathbf{k}$. Finally, the incoming-wave-normalized hyperspherical channel wave function $\Psi^-_{\mu k}$ in Eq. (16) is given by

$$\Psi^-_{\mu k}(R,\alpha,\hat{\mathbf{r}}_1,\hat{\mathbf{r}}_2) = [R^{5/2}\cos(\alpha)\sin\alpha]^{-1}\Phi_\mu(R,\alpha,\hat{\mathbf{r}}_1,\hat{\mathbf{r}}_2) \times F_{\mu k}(R)e^{-i\eta_\mu} . \tag{18}$$

Note that the form of this final-state wave function differs from that of the initial-state wave function in Eq. (15) by the incoming-wave-normalization phase factor, where η_μ is the phase shift in the channel μ relative to the analytically known long-range dipole-field phase ξ_μ. The asymptotic form of $F_\mu(R)$ is given in Eq. (7).

Substituting Eqs. (15), (16), and (18) in Eq. (13) [as well as an expression similar to Eq. (15) for Ψ_{μ_r}], we may express the two-photon transition amplitude as

$$T^{(2)}_{nlm\mathbf{k}} = k^{-1/2}\sum_{l',m'}\sum_{L,M} Y_{l'm'}(\hat{\mathbf{k}})\langle lml'm'|LM\rangle X^{(2)LM}_{nl,kl'} , \tag{19}$$

where $X^{(2)LM}_{nl,kl'}$ is the amplitude for the resonant two-photon electric dipole transition from the initial state to a final state of angular momentum LM characterized by the hydrogen atom in the nl state and by the detached electron having wave number k and orbital angular momentum l'. Specifically,

$$X^{(2)LM}_{nl,k\ell'} \equiv -i2\Gamma_r^{-1}\sum_\mu A_{(ll'),\mu}\ \exp i(\xi_\mu+\eta_\mu)\int_0^\infty dR\, F_{\mu k}\,(R)R\, I^{q'}_{\mu\mu_r}\,(R)F_{\mu_r}(R) \times\int_0^\infty dR'\, F_{\mu_r}\,(R')R'\, I^{q}_{\mu_r 0}\,(R')F_0(R') . \tag{20}$$

In Eq. (20), $I^q_{\mu\mu'}(R)$ is the five-dimensional angular integral of the dipole operator in Eq. (14) between the channel functions $\Phi_\mu(R;\alpha,\hat{\mathbf{r}}_1,\hat{\mathbf{r}}_2)$ and $\Phi_{\mu'}(R;\alpha,\hat{\mathbf{r}}_1,\hat{\mathbf{r}}_2)$. For linearly polarized light (i.e., $q=0$) this angular integral is defined explicitly in Eq. (9) of Ref. [16]. For other values of the light polarization, one may obtain $I^q_{\mu'\mu}$ in terms of a reduced angular integral $I_{\mu\mu'}(R)$, which is defined by the Wigner-Eckart theorem as follows:

$$I^q_{\mu\mu'}(R) \equiv (-1)^{L_\mu - M_\mu}\begin{pmatrix} L_\mu & 1 & L_{\mu'} \\ -M_\mu & q & M_{\mu'}\end{pmatrix} I_{\mu\mu'}(R) . \tag{21}$$

Expressing $I^{q'}_{\mu\mu_r}$ and $I^q_{\mu_r 0}$ in Eq. (20) in terms of their reduced matrix elements [cf. Eq. (21)], we may similarly write the amplitude $X^{(2)LM}_{nl,kl'}$ in terms of an amplitude $X^L_{nl,kl'}$, which is independent of magnetic quantum numbers, as follows:

$$X^{(2)LM}_{nl,kl'} \equiv (-1)^{L-M+L_r-M_r}\begin{pmatrix} L & 1 & L_r \\ -M & q' & M_r\end{pmatrix} \times\begin{pmatrix} L_r & 1 & 0 \\ -M_r & q & 0\end{pmatrix} X^L_{nl,kl'} . \tag{22}$$

Equation (22) permits one to easily examine the dependence of the photodetached-electron angular distributions on the polarizations q and q' of the two photons, as we show next.

B. Differential cross sections

The differential cross sections for two-color, two-photon detachment of the $^1S^e$ ground state of H^- with excitation of the H($2l$) state (i.e., $2s$ or $2p$) are given by

$$\frac{d\sigma^{2\ell}}{d\Omega} = 8\pi^3\alpha^2\omega\omega' k\sum_m |T^{(2)}_{2lm\mathbf{k}}|^2 , \tag{23}$$

where $T^{(2)}_{2lm\mathbf{k}}$ is defined by Eqs. (19) and (20). Substituting Eq. (22) in Eq. (19) and using standard angular momentum algebra [17], the summations over magnetic quantum numbers may be performed to obtain

$$\frac{d\sigma^{2\ell}}{d\Omega} = \frac{1}{4\pi}\sum_{j=0}^{2}\sigma^{2\ell}_{2j}\,P_{2j}(\cos\theta_{\hat{\mathbf{k}}}) , \tag{24}$$

where

$$\sigma_K^{2\ell}(q,q') = \frac{8\pi^3\alpha^2\omega\omega'}{3}\sum_{\ell'\ell''}\sum_{LL'}(-1)^{\ell+q+q'}\left(\frac{[L,L',\ell',\ell'',K]}{4\pi}\right)^{1/2}\begin{pmatrix} L & 1 & 1\\ -(q+q') & q' & q\end{pmatrix}\begin{pmatrix} L' & 1 & 1\\ -(q+q') & q' & q\end{pmatrix}$$
$$\times\begin{pmatrix} L & K & L'\\ q+q' & 0 & -(q+q')\end{pmatrix}\begin{pmatrix}\ell' & \ell'' & K\\ 0 & 0 & 0\end{pmatrix}\begin{Bmatrix} L & K & L'\\ \ell'' & \ell & \ell'\end{Bmatrix} X^L_{nl,kl'}\left(X^{L'}_{nl,kl''}\right)^\dagger . \quad (25)$$

In Eq. (25) we have used the notation $[a,b,\ldots] = (2a+1)(2b+1)\ldots$. For $K=0$, we obtain the total cross section,

$$\sigma_0^{2\ell}(q,q') = \frac{8\pi^3\alpha^2\omega_1\omega_2}{3(4\pi)^{1/2}}\sum_{\ell',L}\begin{pmatrix} L & 1 & 1\\ -(q+q') & q' & q\end{pmatrix}^2 \times\left|X^L_{nl,kl'}\right|^2 . \quad (26)$$

C. Circular dichroism cross sections

With Eq. (25) in hand, it is easy to examine the possibility of circular dichroism (CD) in the angular distributions for process (1) [7]. Consider first the case in which the first photon is linearly polarized, i.e., $q=0$. The polarization axis for this photon determines the z axis. The second photon is assumed to be right- or left-circularly polarized along this axis, i.e., $q' = \pm 1$. Inspection of Eq. (25) and use of standard symmetry properties of $3j$ symbols show that

$$\sigma_K^{2\ell}(q=0,q'=+1) = \sigma_K^{2\ell}(q=0,q'=-1) . \quad (27)$$

Hence in this case there is no CD effect.

Consider, however, the case in which the first photon is right-circularly polarized, i.e., $q=+1$. If the second photon is also circularly polarized along the same axis, then Eq. (25) shows that there is a CD effect since for $K=0$ and $K=2$

$$\Delta\sigma_K^{2\ell} \equiv \sigma_K^{2\ell}(q=+1,q'=+1) - \sigma_K^{2\ell}(q=+1,q'=-1) \neq 0 . \quad (28)$$

The advantage of considering the CD cross section is that it gives a simplified angular distribution. By inspection of Eq. (25) one may verify that

$$\Delta\sigma_{K=4}^{2\ell} = \sigma_{K=4}^{2\ell}(q=+1,q'=+1) - \sigma_{K=4}^{2\ell}(q=+1,q'=-1) = 0 . \quad (29)$$

Thus the CD differential cross section has only constant and $\cos^2\theta_{\hat{\mathbf{k}}}$ terms; there are no higher powers of $\cos\theta_{\hat{\mathbf{k}}}$.

IV. RESULTS

We present here our semiempirical adiabatic hyperspherical results for the resonant two-color detachment process (1). We examine the cases in which the two photons are respectively linearly and circularly polarized, both right-circularly polarized, and right- and left-circularly polarized. In all cases the two photons have the same polarization axis, which we take to be the z axis. We also examine the circular dichroism cross section for the case in which the first photon is right-circularly polarized and the second photon is alternately right- and left-circularly polarized.

A. Numerical aspects

In our semiempirical adiabatic hyperspherical treatment, we have adjusted the lowest-energy ^1S adiabatic hyperspherical radial potential $V_{\mu=0}(R)$ [cf. Eq. (4)] so that the total ground-state energy E_g for H^- agrees with the nonrelativistic energy predicted by Pekeris [18], i.e., $-0.527\,751$ a.u. This compares with the adiabatic hyperspherical value of $-0.525\,917$ a.u. The adjustment of $V_\mu(R)$ is accomplished by deepening the bottom of the well very slightly, and smoothly joining the deepened part onto the adiabatic hyperspherical potential by a spline procedure. No correction to the angular function $\phi_{\mu=0}$ for the ^1S channel was made.

A similar semiempirical adjustment was made for the $\mu_r = {}^1P^o-$ radial potential $V_{\mu_r}(R)$ so that the so-called $2s3p\,{}^1P^o$ Feshbach resonance has the energy $-0.126\,049\,8$ a.u. predicted by Ho [19]. This compares with the adiabatic hyperspherical energy of $-0.125\,892\,7$ a.u. We have also employed Ho's width for this resonance of $\Gamma_r = 1.32\times10^{-6}$ a.u. [19]. As shown in Ref. [19], there appears to be theoretical agreement on the resonance energy. Such is not the case, however, for the resonance width. We have selected Ho's value since it is one of the most recent and also since it is consistent with earlier work of Callaway [20].

Our potentials $V_\mu(R)$ and angle functions ϕ_μ were only calculated numerically for $R \le 40$ a.u. In the range 40 a.u. $\le R \le 200$ a.u., the analytically known asymptotic forms for these functions [8] were used. A spline fit was used to join the numerical and analytic values of quantities dependent on $U_\mu(R)$ and ϕ_μ in the vicinity of $R \approx 40$ a.u.

Finally, we note here our estimate of the possible effect of nonadiabatic couplings on our initial-state wave function. The H^- ground-state radial wave function has been calculated by Sadeghpour [21] both with and without coupling to the next higher $^1S^e$ channel. Below the wave function maximum at R=3.099 a.u., the two wave functions differ by much less than 1%. At the maximum, they differ by about 0.3%. Above the maximum, between 10 and 15 a.u. where the wave function is decreasing in magnitude, the two wave functions differ by about 5%. Now, in the exponential tail region the ground-state energy determines the behavior of the wave function. Because our semiempirical radial wave function is adjusted to have the correct energy eigenvalue, it is superior to either of these two *ab initio* wave functions in the exponential tail region. Otherwise, on the basis of these calculations [21], it is probably fair to say that our radial

wave function is correct to within a few percent. Therefore, our cross-section predictions certainly will not be affected significantly as a result of our neglect of nonadiabatic coupling in the initial state.

B. Use of QDT to examine long-range dipole-field effects

As discussed in Sec. II B, there are two major ways in which attractive, long-range dipole fields introduce oscillations in measured cross sections on a $\ln k$ energy scale. The first is due to the analytically known dipole phases ξ_μ and θ_μ, which are defined in Eqs. (9) and (10). These phases enter the amplitudes $X^{(2)LM}_{n\ell,k\ell'}$ defined in Eq. (20). Interference effects between different amplitudes, such as commonly occur in the differential cross sections [cf. Eqs. (24) and (25)], generally lead to sizable undamped oscillations in these cross sections, due to the rapid decrease of the phase shifts θ_μ with increasing $\ln k$, as shown in Fig. 2.

The second major way that attractive, long-range dipole fields introduce oscillations in measured cross sections on a $\ln k$ energy scale is through the effective normalization factor $N_\mu(k)$ [cf. Eq. (12) and Fig. 3]. $N_\mu(k)$ is defined as follows [14]:

$$N_\mu(k) = [\, B_\mu \cos^2\eta_\mu + B_\mu^{-1}(1+\mathcal{G}_\mu^2)\sin^2\eta_\mu - \mathcal{G}_\mu \sin(2\eta_\mu)]^{1/2} , \tag{30}$$

where η_μ is the phase shift in the μth channel [cf. Eq. (7)] and where B_μ and $\mathcal{G}_\mu$ are analytic functions defined by [12]

$$B_\mu = \frac{\sinh(\pi\alpha_\mu)}{\cosh(\pi\alpha_\mu) - \cos\{2[\alpha_\mu \ln(k/2) + x_\mu]\}} , \tag{31}$$

$$\mathcal{G}_\mu = \frac{-\sin\{2[\alpha_\mu \ln(k/2) + x_\mu]\}}{\cosh(\pi\alpha_\mu) - \cos\{2[\alpha_\mu \ln(k/2) + x_\mu]\}} . \tag{32}$$

The parameters α_μ and x_μ are defined in Eqs. (6) and (11).

A third, usually rather minor, way that attractive, long-range dipole fields introduce oscillations in measured cross sections on a $\ln k$ energy scale is through the phase shift η_μ [cf. Eq. (7)]. This phase may be expressed in terms of a smooth, short-range phase η_μ^0 as follows [14]:

$$\tan\eta_\mu = \frac{B_\mu \tan\eta_\mu^0}{1 + \mathcal{G}_\mu \tan\eta_\mu^0} . \tag{33}$$

Here B_μ and $\mathcal{G}_\mu$ are defined in Eqs. (31) and (32). For large values of α_μ, $B_\mu \to 1$ and $\mathcal{G}_\mu \to 0$ so that $\eta_\mu \to \eta_\mu^0$. In this case, we also see from Eq. (30) that $N_\mu \to 1$. For finite values of α_μ, however, both B_μ and $\mathcal{G}_\mu$ oscillate on a scale of $\ln k$, thereby introducing oscillations in both $N_\mu(k)$ and η_μ. However, whereas $N_\mu(k)$ affects both total as well as differential cross sections, η_μ affects only differential cross sections through phase-interference effects between different amplitudes. Furthermore, since it appears together with the analytically known phase ξ_μ [cf. Eq. (20)], its effect is subsidiary to that of ξ_μ.

We compare η_μ and η_μ^0 in Fig. 4 for the two most important final-state channels in the present calculations, $\mu = {}^1D+$ and $\mu = {}^1S(K{=}+1)$. One sees clearly that the oscillations in η_μ for $\mu = {}^1D+$ are of much larger amplitude than are those for $\mu = {}^1S(K{=}+1)$. This is similar to the relative amplitude of oscillations of the effective normalization factors $N_\mu(k)$ for these two channels, as shown in Fig. 3. Indeed, for both $N_\mu(k)$ and $\eta_\mu(k)$, the primary source of oscillatory behavior stems from the function B_μ in Eq. (31) [4]. Neglecting terms of order $\exp(-2\pi\alpha_\mu)$ compared to 1, B_μ in Eq. (31) may be approximated by

$$B_\mu \approx (1 - 2e^{-\pi\alpha_\mu}\cos\{2[\alpha_\mu \ln(k/2) + x_\mu]\})^{-1} . \tag{34}$$

Hence, one sees clearly that the amplitude factor $2e^{-\pi\alpha_\mu}$ for the oscillatory cosine term is in general likely to be small. This suppression of the dipole-field-induced oscillations above threshold was first pointed out by Fabrikant [3] and was analyzed in detail for single-photon photodetachment of H^- with excitation of the residual H atom by Greene and Rau [4]. However, Liu, Du, and Starace [6] found that the ${}^1D+$ potential converging to the H($n = 2$)

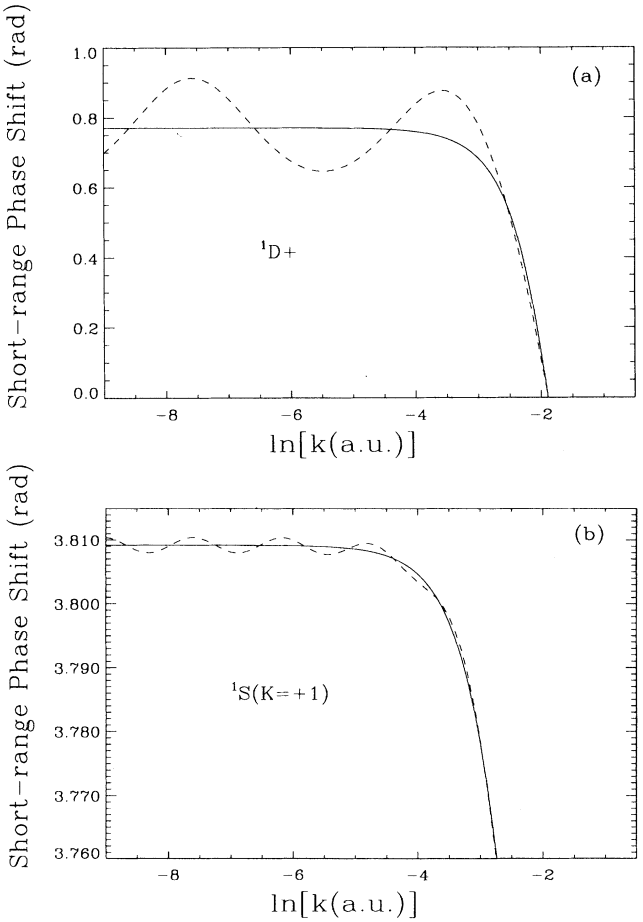

FIG. 4. Short-range phase shifts for two attractive long-range dipole-field channels μ: (a) $\mu = {}^1D+$. (b) $\mu = {}^1S(K{=}+1)$. The dashed lines show the phase shifts η_μ [cf. Eq. (7)] and the solid lines show the smooth phase shifts η_μ^0 [cf. Eq. (33)].

threshold has an unusually small value of α_μ equal to 0.748. This gives an amplitude factor $2e^{-\pi\alpha_\mu}$ equal to 0.19. This behavior of the $^1D+$ channel contrasts with the α_μ value of 2.2 and the amplitude factor value of 0.002 for the $^1S(K=+1)$ channel. In the Appendix we indicate all channels of the H(n)-e^- system for which the amplitude factor exceeds the value 0.1. There are only eight such channels for principal quantum numbers n in the range $2 \leq n \leq 15$ and total orbital angular momenta L in the range $0 \leq L \leq 3$.

Our procedure for demonstrating effects of the long-range dipole field as contrasted to other dynamical effects is as follows. In the figures that follow, the solid curves give our semiempirical adiabatic hyperspherical results. The dashed curves indicate what these results would be if the long-range dipole field were removed. These are calculated by dividing each $F_{\mu k}(R)$ final-state radial function in the amplitude in Eq. (20) by the normalization factor $N_\mu(k)$. For the total cross sections σ_0 in Eq. (26) this is sufficient to remove all of the oscillatory energy dependence for $\ln k \lesssim -4$. For the other components of the differential cross sections (namely, σ_2 and σ_4 [cf. Eq. (25)]) one must also remove the dipole-field-induced energy dependence of both the analytically known phase shift θ_μ [cf. Eq. (10)] and the phase shift η_μ [cf. Eq. (33)]. As noted already, these phases enter into the expressions for the transition amplitudes in Eq. (20). For this purpose, θ_μ is fixed to its value at $\ln k = -9$; η_μ is simply replaced by η_μ^0. When these phases are so treated, the dashed curves for σ_2 and σ_4 [cf. Eq. (25)] also become constant in energy for $\ln k \lesssim -4$.

C. Results

We present our calculated cross-section results for the two-color detachment process (1) for various pairs of light polarization on a scale of $\ln k$ in order to demonstrate clearly the predicted long-range dipole-field-induced oscillations. Conversion of $\ln k$ to detached electron kinetic energy $k^2/2$ is given in Table I. As indicated in Table I, the assumption of degeneracy in the $n = 2$ level of H breaks down due to the spin-orbit interaction and the Lamb shift at values of $\ln k \lesssim -6$. We have nevertheless plotted our results over the region $\ln k \geq -9$ in order to exhibit at least one full cycle of the oscillatory behavior expected above threshold under the assumption that the $n = 2$ levels are degenerate.

In general, the resonant cross sections presented here are eight to nine orders of magnitude larger than the nonresonant two-photon detachment cross-sections presented in Ref. [6]. However, a price paid for this increased cross-section magnitude near threshold is a reduced energy region over which the long-range dipole-field-induced oscillations are unmistakable. The reason for this is that the resonant intermediate Feshbach state is so close to the H($n = 2$) threshold that it has a very broad spatial extension. Hence, the radial integral for dipole transitions to the final state becomes sensitive to the detached electron's kinetic energy at much lower values of kinetic energy *even in the absence of long-range dipole-field effects*. Furthermore, cancellation in this dipole radial integral becomes so severe by $\ln k = -2$ (250 meV) that the predicted cross sections are effectively zero on the cross-section scale shown. However, this nondipole-field energy-dependence is rather minor over the 5-meV energy region $-6 \leq \ln k \lesssim -4$. In addition, by examination of the photodetached electron angular distribution and, most importantly, circular dichroism cross sections, this nondipole-field energy dependence may be shown to be minor over a much larger energy region, sometimes exceeding even the 34-meV energy region above threshold that was predicted for the nonresonant two-photon cross sections in Ref. [6].

TABLE I. Comparison of $\ln k$ versus electron energy $k^2/2$.

$\ln k$ (a.u.)	$k^2/2$ (eV)
−9.0	2.1×10^{-7}
−8.0	1.5×10^{-6}
−7.5	4.3×10^{-6} [a]
−7.0	1.1×10^{-5}
−6.3	4.5×10^{-5} [b]
−6.0	8.4×10^{-5}
−5.0	6.2×10^{-4}
−4.0	4.6×10^{-3}
−3.0	3.4×10^{-2}
−2.0	2.5×10^{-1}
−1.0	1.8
−0.5	5.0

[a] Magnitude of $2s_{1/2}$-$2p_{1/2}$ Lamb shift.
[b] Magnitude of $2p_{1/2}$-$2p_{3/2}$ spin-orbit splitting.

Note that the rapid decrease of all cross sections by several orders of magnitude for $\ln k > -2$ makes this energy region uninteresting for the purposes of the present paper. For this reason we present the differential cross-section parameters σ_0, σ_2, and σ_4 themselves [cf. Eqs. (24)–(26)] rather than their ratios, the asymmetry parameters $\beta_K \equiv \sigma_K/\sigma_0$.

In all cases, the first photon is resonant with the $2s3p\,^1P^o$ Feshbach resonance. It therefore has an energy $\omega_1 = 0.401\,70$ a.u. The second photon scans the energy region above the H($n = 2$) threshold. Hence $\omega_2 \geq 0.126\,05$ a.u.

1. Linear plus circularly polarized photons

Here we assume that the two light beams are orthogonal. The first is linearly polarized with its polarization vector determining the z axis. The second photon beam is assumed to be right-circularly polarized along this z axis. (However, identical results are obtained if left-circular polarization is assumed, as discussed in Sec. III C.) Electric dipole selection rules permit both $^1D^e$ and $^1P^e$ final states but not $^1S^e$ ones. Furthermore, the $^1P^e$ final states are possible only when the H atom is left in the $2p$ state.

For the case in which the H atom is left in the H($n = 2$) state [=H($2s$) + H($2p$)], we present the differential cross section defined in Eq. (24) for various angles of photoelectron detection in Fig. 5(a). The total cross sections for leaving the H atom in the H($2s$), H($2p$), or H($n = 2$)

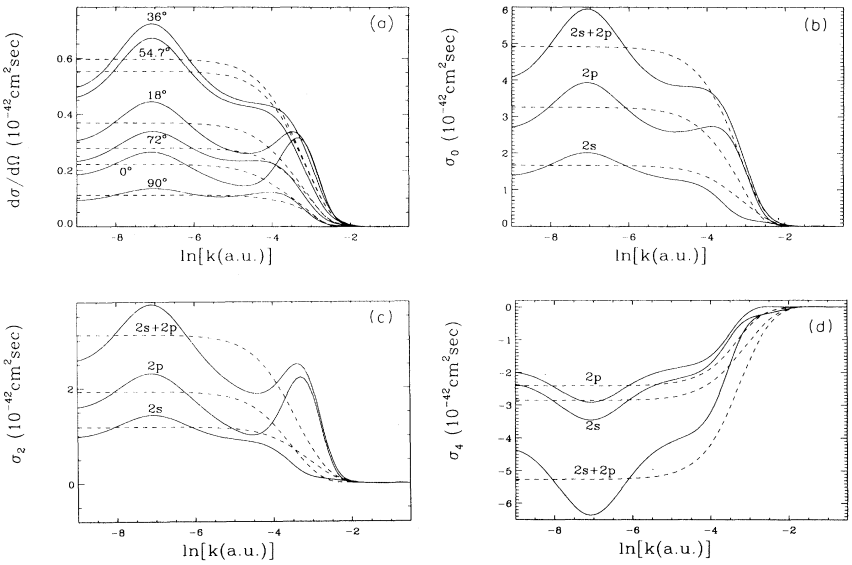

FIG. 5. Generalized cross sections for the process $H^- + \gamma_L + \gamma'_C \rightarrow H(n = 2) + e^-$. (a) Differential cross sections [cf. Eq. (24)] for $H(n = 2) = H(2s) + H(2p)$ final states. (b) Total cross sections [cf. Eq. (26)]. (c) σ_2 [cf. Eqs. (24) and (25)]. (d) σ_4 [cf. Eqs. (24) and (25)]. Solid curves give present results. Dashed curves give present results with long-range dipole-field effects removed using quantum-defect theory (cf. Sec. IV B).

states are shown in Fig. 5(b). Finally, the corresponding angular distribution parameters σ_K for $K = 2$ and 4 [cf. Eq. (24)] are shown respectively in Figs. 5(c) and 5(d).

One sees for this combination of light polarizations that the most dramatic differences between the full curves (which include long-range dipole-field effects) and the corresponding dashed curves (which do not) occur for $\sigma^{2p}_{K=2}$, which has a very strong dipole-field-induced oscillation over the 34-meV range from $-6 \leq \ln k \leq -3$ [cf. Fig. 5(c)]. Similar striking effects are seen also in the differential cross section for producing the $H(n = 2)$ state for photoelectron angles 0° and 18° [cf. Fig. 5(a)]. In contrast, the total cross sections show rather weak dipole-field oscillations in the region $\ln k > -6$ over which the theory is valid [cf. Fig. 5(b)].

2. *Two right-circularly polarized photons*

Here we assume that the two photon beams are right-circularly polarized and that they are copropagating along the same z axis. Because electric dipole selection rules only permit the population of $^1D^e$ final states in this case, the possibility of observing significant interference effects in the differential cross sections is severely reduced. This is so because only the $\mu = {}^1D^e+$ channel has a significant magnitude; the other $^1D^e$ channels are much weaker. Our results are shown in Fig. 6. One sees that the difference between our solid curves (which include long-range dipole-field effects) and our dashed curves (which do not) is not dramatic in the energy range above $\ln k > -6$ over which the theory is applicable.

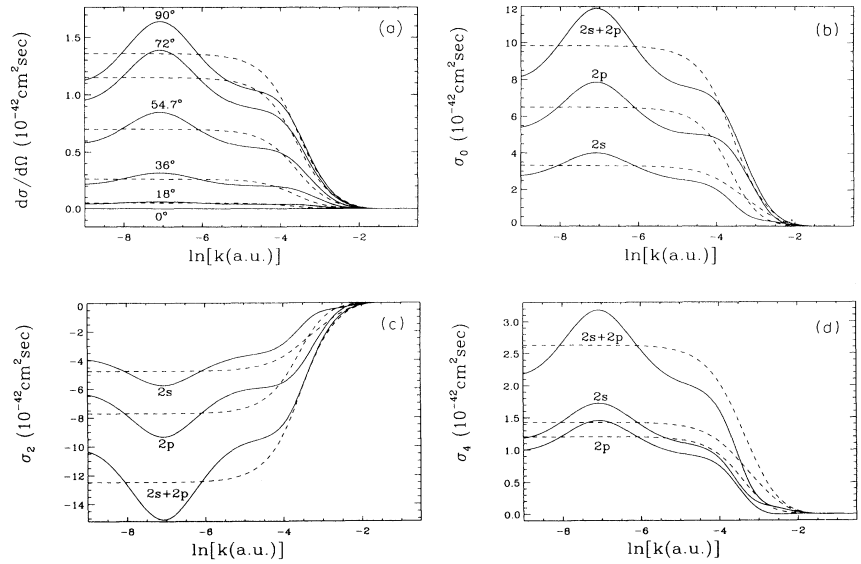

FIG. 6. Generalized cross sections for the process $H^- + \gamma_{C(R)} + \gamma'_{C(R)} \rightarrow H(n = 2) + e^-$. The arrangement of the figure and the labeling of curves are identical to those of Fig. 5.

However, we present these results, nevertheless, as they are needed to understand our circular dichroism results shown below.

3. *Right- and left-circularly polarized photons*

Here we assume that the two photon beams are right- and left-circularly polarized and that they are copropagating along the same z axis. In this case, $M_L = 0$ in the final state and hence electric dipole selection rules permit all $^1D^e$, $^1P^e$, and $^1S^e$ final-state channels to contribute. Furthermore, interference effects can be observed in the differential cross sections for both H($2p$) and H($2s$) final states: for the former, all final states contribute, and, for the latter, both $^1D^e$ and $^1S^e$ channels contribute.

Figure 7(c) shows that the interference effects on σ_2 are very dramatic. It is this component of the differential cross section that gives the differential cross section in Fig. 7(a) its dramatic behavior. Note that σ_4 for this polarization case is not shown, as it is identical to that for the case of two right-circularly polarized photons, which is shown in Fig. 6(d), as has been discussed in Sec. III C. Equality of the σ_4 coefficients for these two different cases of light polarization stems in part from the fact that only the $^1D^e$ channels contribute to σ_4.

4. *Circular dichroism cross sections*

The circular dichroism differential cross section $\Delta(d\sigma/d\Omega)$, given analytically in Eq. (28), is presented in Fig. 8(a). This cross section is obtained by subtracting the generalized cross sections for right- and left-circularly polarized photons [cf. Fig. 7(a)] from those for two right-circularly polarized photons [cf. Fig. 6(a)]. As discussed above, σ_4 is the same for these two cases, so that the circular dichroism differential cross section has $\Delta\sigma_4 = 0$. Finally, the corresponding circular dichroism total cross sections $\Delta\sigma_0$ and $K = 2$ components $\Delta\sigma_2$ are shown in Figs. 8(b) and 8(c), respectively.

For $\theta_{\hat{\mathbf{k}}} = 36°$, the circular dichroism differential cross section is close to oscillating about the value zero, thus implying near cancellation of the average differential cross sections in Figs. 6(a) and 7(a) at this angle. Such cancellation permits one to observe an enhancement of the long-range, dipole-field-induced oscillations. In Fig. 9 we have plotted $\Delta(d\sigma/d\Omega)$ for the final states, H($n = 2$), H($2p$), and H($2s$) at angles for which the cross sections appear to be oscillating about zero in the energy range $\ln k \geq -6$. For the H($2s$) final state at an angle of $\theta_{\hat{\mathbf{k}}} = 37.55°$, in particular, the cross section shown by the dashed line (for which long-range dipole-field effects have been removed) appears to be almost constant as a function of $\ln k$, with value zero. In any case, the actual circular dichroism differential cross section has almost a full cycle of oscillation in the energy region $\ln k \geq -6$.

Now, we hasten to add that the precise value of the average (dashed-line) circular dichroism differential cross section depends on the fact that we have fixed the analytically known phase shifts $\theta_\mu(k)$ [cf. Eq. (10)] at their values at $\ln k = -9$ (-8.5 in the case of Fig. 5). Changing the value of $\ln k$ at which these parameters are fixed in value would have a negligible effect on the value of the average cross section for the case of two right-circularly polarized photons shown in Fig. 6 for angles near 36° since the dashed and solid curves are already very close together. It would have a significant effect on the average value of the cross section for the case of right- and left-circularly polarized photons shown in Fig. 7, however,

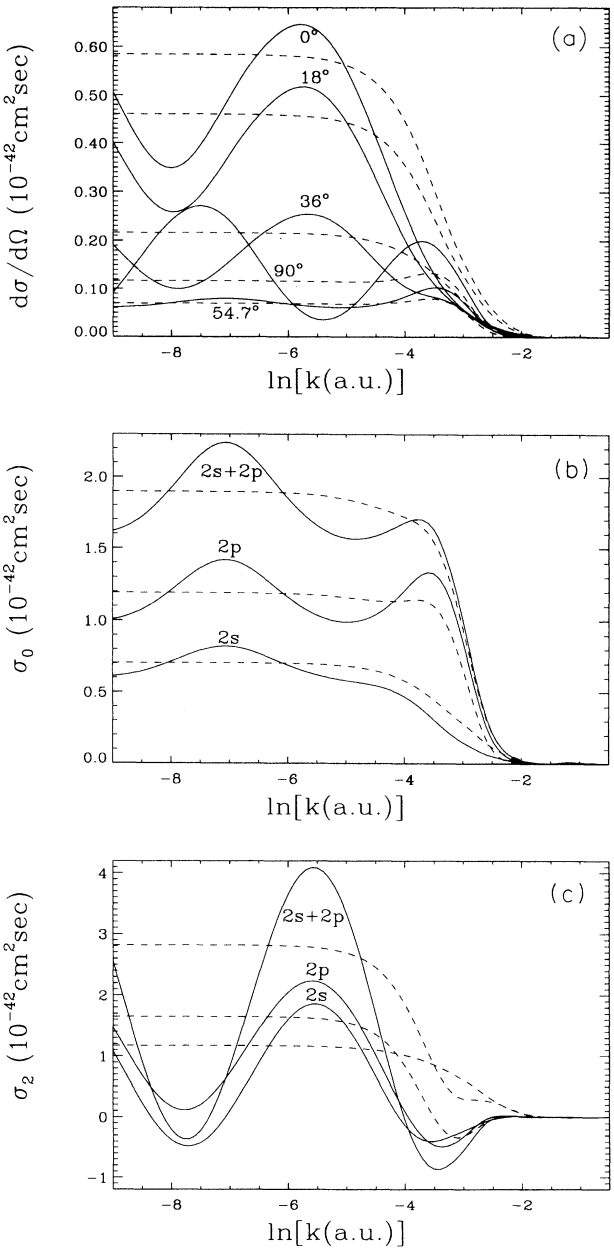

FIG. 7. Generalized cross sections for the process $H^- + \gamma_{C(R)} + \gamma'_{C(L)} \rightarrow H(n = 2) + e^-$. The arrangement of the figure and the labeling of curves are identical to those of Figs. 5(a)–5(c). Note that σ_4 for this case is identical to σ_4 presented in Fig. 6(d) for the case of two right-circularly polarized photons.

since the solid curves have such a large amplitude of oscillation. Nevertheless, the angular region over which the circular dichroism differential cross sections can possibly oscillate about the value zero is very restrictive, as careful comparison of Figs. 6(a) and 7(a) demonstrates. Furthermore, as Fig. 9 indicates, the measurable differential cross sections (solid lines) in the vicinity of 36° have a very different and much more dramatic energy dependence than do the hypothetical cross sections (dashed curves) from which the long-range dipole-field energy dependence has been removed. In particular, the positive-sloped curves in the $\approx$ 5-meV energy region from $-5.5 \leq \ln k \leq -4$ are unmistakable evidence of the long-range, dipole-field-induced cross-section oscillations.

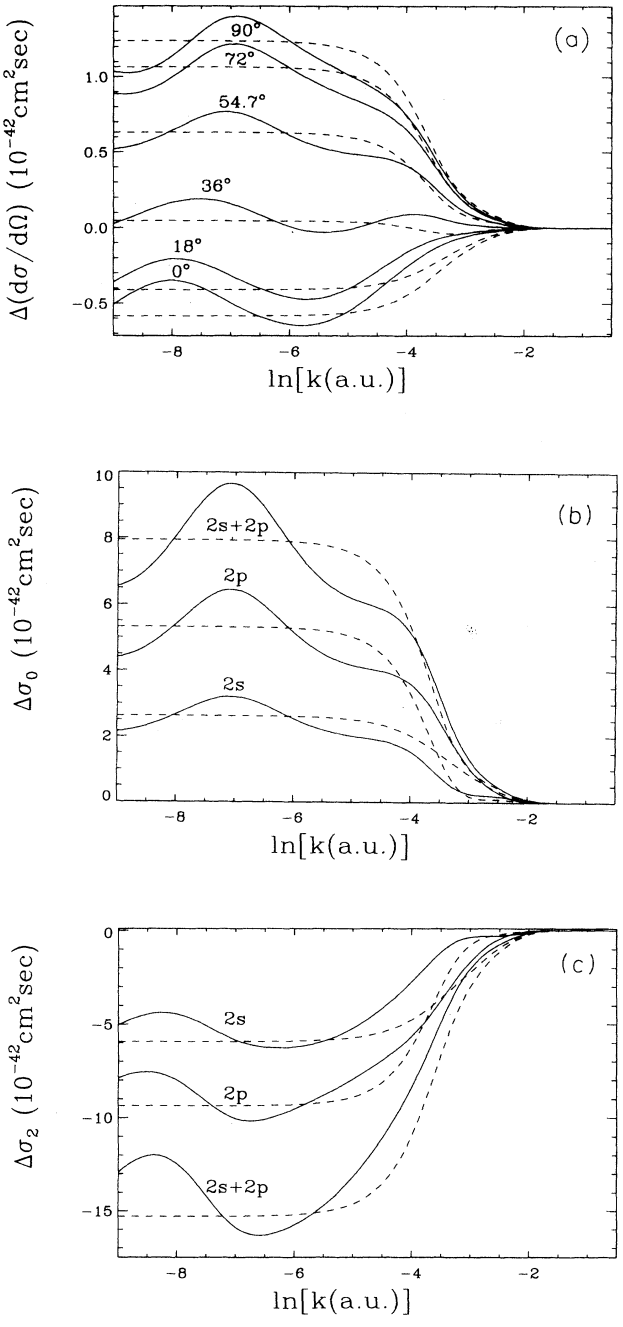

FIG. 8. Generalized circular dichroism cross sections for the process $H^- + \gamma_{C(R)} + \gamma'_{C(R,L)} \rightarrow H(n = 2) + e^-$. The results in Figs. 8(a)–8(c) are obtained by subtracting the results in Figs. 7(a)–7(c) from those in Figs. 6(a)–6(c).

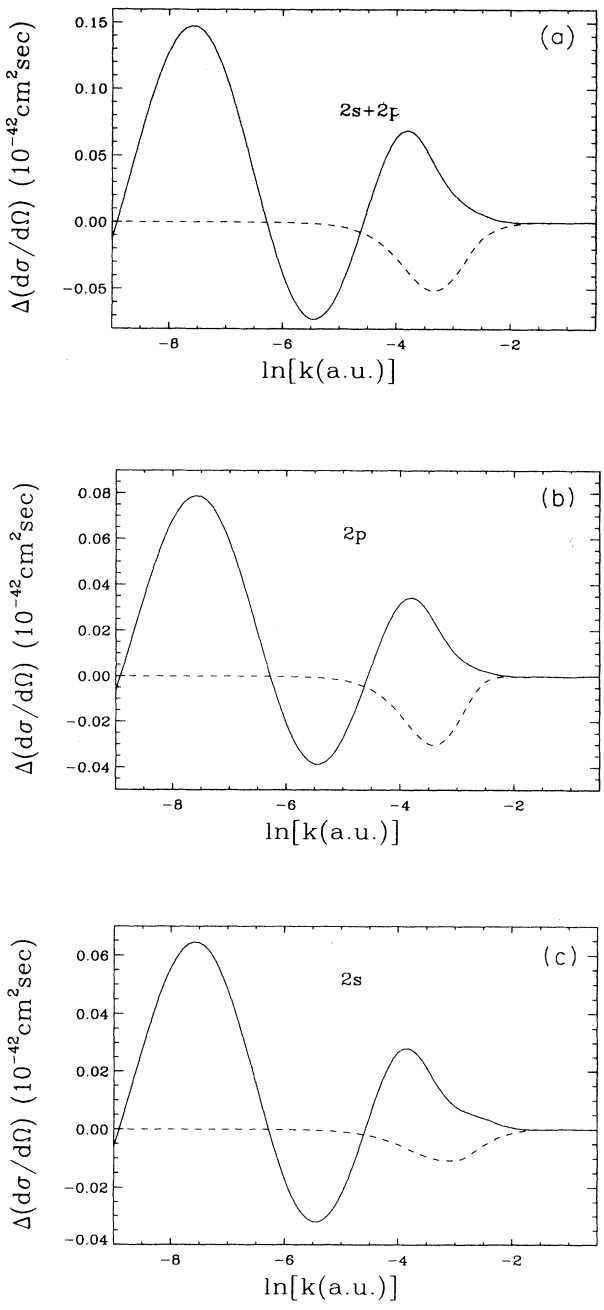

FIG. 9. Generalized circular dichroism differential cross sections at angles for which the cross sections oscillate about the value zero. (a) H($n = 2$) final state for $\theta_{\hat{\mathbf{k}}} = 34.47°$. (b) H($2p$) final state for $\theta_{\hat{\mathbf{k}}} = 32.46°$. (c) H($2s$) final state for $\theta_{\hat{\mathbf{k}}} = 37.55°$.

V. DISCUSSION AND CONCLUSIONS

It has been 30 years since Gailitis and Damburg [2] predicted that attractive, long-range dipole fields produce oscillations in near-threshold cross sections on a scale of $\ln k$, where k is the momentum of an electron scattered by the field. Such oscillations have yet to be observed experimentally, for reasons discussed in Sec. II. Liu, Du, and Starace [6] predicted theoretically that the process of two-photon detachment of H^- with excitation of H($n = 2$) is probably the most likely process for observing such oscillations experimentally. They calculated the cross sections for nonresonant two-photon detachment plus excitation of H^- and predicted that the long-range dipole field produces a half-cycle of oscillation over an energy range from threshold to 34 meV above. However, since the process they calculated is nonresonant, the cross sections are small.

In this paper we have presented theoretical calculations of the two-color, two-photon detachment of H^- with excitation of H($n = 2$) in which the first photon is resonant with the well-known Feshbach $^1P^o$ resonance below the H($n = 2$) threshold. We have also presented results for various pairs of polarization states for the two photons. We find that our resonant cross sections are 10^8–10^9 times larger than those of the corresponding nonresonant cross sections of Ref. [6]. However, because the Feshbach state has such a large radial extent, we find that the range over which long-range dipole-field oscillations are unmistakable is reduced to about 5 meV. Nevertheless, studies of differential cross sections and, in particular, of circular dichroism cross sections give more prominent long-range dipole-field effects. In particular, there is nearly a full cycle of oscillation in these cross sections over the 34-meV energy region $-6 \leq \ln k \leq -3$. This fact, combined with the much larger cross sections, may make the resonant process considered in this paper an interesting alternative to the nonresonant process of Ref. [6] for experimentalists planning to observe these effects for the first time.

ACKNOWLEDGMENTS

A.F.S. thanks Dr. Hossein Sadeghpour for helping to estimate the magnitude of the nonadiabatic interactions on our ground-state wave function. He also gratefully acknowledges the partial support of the JILA Visiting Fellowship Program. N.A.C. is greatly indebted to the University of Nebraska-Lincoln for financial support and for the hospitality extended to him during his stay. This work was supported in part by the U.S. Department of Energy, Office of Basic Energy Sciences, Division of Chemical Sciences, under Grant No. DE-FG02-88ER13955.

APPENDIX

The purpose of the Appendix is to demonstrate which other channels of the H(n)-e^- three-body system may be expected to have significant long-range dipole-field oscillations. As the discussion concerning Eq. (34) of this paper indicates, the key indicator of the magnitude of such oscillations is the amplitude factor $2e^{-\pi\alpha_\mu}$, where α_μ is the complex part of the effective angular momentum λ_μ [cf. Eq. (6)] when the long-range part of the effective potential is attractive [cf. Eq. (15)]. In order to calculate α_μ, one may start from an independent electron representation.

TABLE II. Dipole potential strengths $[\lambda_\mu(\lambda_\mu + 1)]$, complex parts of $\lambda_\mu(\alpha_\mu)$, and oscillatory amplitudes $(2e^{-\pi\alpha_\mu})$ for all channels ^1L of the H(n)-e^- system for which the amplitudes are greater than 0.1. All values of n in the range $2 \leq n \leq 15$ and all values of L in the range $0 \leq L \leq 3$ were considered.

n	Term (^1L)	$\lambda_\mu(\lambda_\mu + 1)$	α_μ [a]	$2e^{-\pi\alpha_\mu}$
2	$^1D^e$	−0.8102	0.7485	0.1905
4	$^1D^e$	−0.8548	0.7778	0.1738
4	$^1F^e$, $^1F^o$	−0.3434	0.3056	0.7658
5	$^1D^e$, $^1D^o$	−0.4581	0.4562	0.4771
6	$^1D^e$, $^1D^o$	−1.1532	0.9503	0.1010

[a] $\alpha_\mu = [-\lambda_\mu(\lambda_\mu + 1) - 1/4]^{1/2}$.

As shown by Seaton [1], the long-range dipole interaction between an electron at r_2 having angular momentum ℓ' and a bound electron with angular momentum ℓ at $\mathbf{r}_1$, where $r_2 \gg r_1$, is

$$\frac{\mathbf{a}}{r_2^2} \equiv \frac{\ell'(\ell'+1) + 2r_1\cos\theta_{12}}{r_2^2} . \tag{A1}$$

The effective angular momentum λ_μ is determined by diagonalizing the matrix $\mathbf{a}$ in a hydrogenic basis of states having angular momenta ℓ, ℓ' for the two electrons:

$$\mathbf{A}^\dagger\mathbf{a}\mathbf{A} = \boldsymbol{\lambda}(\boldsymbol{\lambda}+\mathbf{1}) , \tag{A2}$$

where the matrix $A_{(\ell\ell'),\mu}$ was introduced in Eq. (16). As shown by Macek [8], the adiabatic hyperspherical potentials have this diagonal form asymptotically [cf. Eq. (5)].

We have carried out the diagonalization of the matrix $\mathbf{a}$ within a basis of coupled hydrogenic states $R_{n\ell}(r_1)$ $Y_{\ell\ell' LM}$ $(\mathbf{r_1}, \mathbf{r_2})$, where $Y_{\ell\ell' LM}$ $(\mathbf{r}_1, \mathbf{r}_2)$ is a product of spherical harmonics coupled to total angular momentum L and component M. Once we obtain those eigenvalues $\lambda_\mu(\lambda_\mu + 1)$ having a value $< -1/4$, we obtain α_μ from

$$\alpha_\mu \equiv [-\lambda_\mu(\lambda_\mu + 1) - 1/4]^{1/2} . \tag{A3}$$

Our results are presented in Table II. We list here all values of n and L that produce an amplitude factor $2e^{-\pi\alpha_\mu} > 0.1$. Our search extended over the range $2 \leq n \leq 15$ and $0 \leq L \leq 3$. The $^1D^e$+ channel converging to H($n = 2$) is the first entry, with an amplitude factor of 0.19. One sees from the table that there are $^1F^e$ and $^1F^o$ channels converging to H($n = 4$), which have an amplitude of 0.77, and that there are $^1D^e$ and $^1D^o$ channels converging to H(n=5), which have an amplitude of 0.48. However, because of the larger radial extent of the H($n = 4$) and H($n = 5$) bound-state wave functions, the energy range above threshold over which such large oscillations may be observed and clearly distinguished from nondipole-field dynamical energy dependences is still an open question.

* Present address: Radiation Oncology Department, William Beaumont Hospital, 3601 West Thirteen Mile Road, Royal Oak, MI 48073-6769.

† Permanent address: Department of Physics and Astronomy, The University of Nebraska, Lincoln, NE 68588-0111.

‡ Permanent address: Aviation Instrument Making Institute, Herzenstrasse 67, 190000 St. Petersburg, Russia.

[1] M. J. Seaton, Proc. Phys. Soc. London **77**, 174 (1961).

[2] M. Gailitis and R. Damburg, Zh. Eksp. Teor. Fiz. **44**, 1644 (1963) [Sov. Phys. JETP **17**, 1107 (1963)]; Proc. Phys. Soc. London **82**, 192 (1963); M. Gailitis, in *Atomic Physics 6*, edited by R. Damburg and O. Kukaine (Plenum, New York, 1978), pp. 249–266.

[3] I. I. Fabrikant, Zh. Eksp. Teor. Fiz. **73**, 1317 (1977) [Sov. Phys. JETP **46**, 693 (1977)].

[4] C. H. Greene and A. R. P. Rau, Phys. Rev. A **32**, 1352 (1985).

[5] (a) C. R. Liu and A. F. Starace, Phys. Rev. Lett. **62**, 407 (1989); (b) Phys. Rev. A **40**, 4926 (1989).

[6] C. R. Liu, N. Y. Du, and A. F. Starace, Phys. Rev. A **43**, 5891 (1991).

[7] N. A. Cherepkov and V. V. Kuznetsov, J. Phys. B **22**, L405 (1989). The related topic of circular dichroism of optically active (chiral) molecules was treated earlier by B. Ritchie, Phys. Rev. A **13**, 1411 (1976); **14**, 359 (1976).

[8] J. Macek, J. Phys. B **1**, 831 (1968).

[9] U. Fano, Rep. Prog. Phys. **46**, 97 (1983).

[10] A. F. Starace, in *Fundamental Processes of Atomic Dynamics*, edited by J. S. Briggs, H. Kleinpoppen, and H. O. Lutz (Plenum, New York, 1988), pp. 235–258.

[11] C. D. Lin, Phys. Rev. Lett. **35**, 1150 (1975).

[12] C. Greene, U. Fano, and G. Strinati, Phys. Rev. A **19**, 1485 (1979).

[13] C. D. Lin, Phys. Rev. A **29**, 1019 (1984); Adv. At. Mol. Phys. **22**, 77 (1986). Specifically, our channels μ converging to the H($n = 2$) level have the following labels in Lin's (K,T)^A notation: $^1S(K = \pm 1)$, $(\pm 1,0)^+$; $^1P+$, $(0,1)^+$; $^1P-$, $(1,0)^-$; $^1P(pd)$, $(-1,0)^0$; $^1D+$, $(1,0)^+$.

[14] U. Fano and A. R. P. Rau, *Atomic Collisions and Spectra* (Academic, New York, 1986), Secs. 5.4 and 5.7.3.

[15] C. R. Liu, N. Y. Du, and A. F. Starace, Phys. Rev. A **43**, 5891 (1991), Sec. IV C.

[16] C. H. Park, A. F. Starace, J. Tan, and C. D. Lin, Phys. Rev. A **33**, 1000 (1986).

[17] The relations needed are similar to those specified in deriving Eq. (30) in Ref. [6].

[18] C. L. Pekeris, Phys. Rev. **126**, 1470 (1962).

[19] Y. K. Ho, Chin. J. Phys. (Taipei) **29**, 327 (1991).

[20] J. Callaway, Phys. Lett. **68A**, 315 (1978). See also unpublished work quoted in Ref. [19].

[21] H. Sadeghpour (private communication).